European Polymer Journal 229 (2025) 113878

Contents lists available at ScienceDirect

European Polymer Journal

journal homepage: www.elsevier.com/locate/europolj

Evaluation of the effect of coupling agent on the kinetic and mechanical properties of a 3D printable dual curing epoxy/acrylate system

A.A. Escriba-Flores [a], X. Fernández-Francos [b], F. Ferrando [a], A. Fabregat-Sanjuan [a,*]

[a] Department of Mechanical Engineering. Universitat Rovira i Virgili. Av. Països Catalans 26, 43007 Tarragona, Spain
[b] Thermodynamics Laboratory, ETSEIB, Universitat Politècnica de Catalunya, Av. Diagonal 647, 08028 Barcelona, Spain

ARTICLE INFO

Keywords:
Dual-Curing
Vat photopolymerization 3D printing
Multi-material
High mechanical performance

ABSTRACT

In recent years, the use of vat photopolymerization in additive manufacturing technology has created a prominent potential in the world manufacturing industry due to its adaptability and quick production capabilities. However, a challenge faced by this technology is creating large-sized parts and ensuring the geometric versatility of processed parts. The physical and mechanical properties of existing materials limit their processing, affecting their final applications. Moreover, dual-curing systems allow new possibilities to 3D printing if shape geometry is changed after the first curing stage and fixed in the second curing stage. This study aims to address these challenges by developing a dual-curing system involving epoxy/acrylic resins. We assess the kinetic and mechanical behavior, focusing on variations in the network coupling agent. The initial curing stage of a low viscous formulation, achieved through processing on a DLP 3D printer (partially cured), produces a flexible material allowing deformations up to 160 %. The second curing stage, achieved through thermal treatment, transforms the material into a rigid system with an impressive maximum tensile strength close to 80 MPa. We compare the contribution of the bonding agent in partial and total cured states. Comprehensive mechanical tests have been performed, including tension and shear evaluations. Results have been favorably aligned with relevant literature. The dual-curing approach shows promise in expanding 3D printing vat photopolymerization applications, providing new design and manufacturing possibilities by enhancing material availability. Our findings emphasize the benefits of the dual-curing system, including low viscosity, shape manipulation during intermediate curing that allows complex geometries with fast procedures and without the need of supports and exceptional strength and durability achieved in the final curing phase. Results on mechanical characterization in joints show that dual curing resins could be attractive in applications where different parts must be joined and precise alignment and structural integrity are crucial. The main reason for that is the interaction with the bonding agent in each state of the dual curing.

1. Introduction

Vat photopolymerization resins in Additive Manufacturing (AM) have generated great interest in the scientific and industrial community, due to its versatility in terms of the facility of generating geometries and structures without the need for a mold or another industrial tool [1–4]. In spite of their advantages, the potential use of this technology to a large extent of the manufacturing industry is still limited by the availability and versatility of the materials present today [5].

Most resin formulations for vat polymerization applications are based on acrylic resins [6–8] and methacrylates [9,10], among others [11], due to their suitable reactivity and wide availability. However, one of the notable limitations of these materials lies in the mechanical properties that they offer; the parts formed by these materials do not promise good structural performance where the demands imply high resistance and durability [12,13]. Conventional systems of photocurable resins for vat polymerization applications are processed in one or two curing stages [14–17]. In the first stage, a photoinitiator is activated under UV or visible light, initiating polymerization and solidifying the monomers/oligomers. The result is either a partially or fully cured material. To improve mechanical properties, advanced systems include a second stage with a thermal initiator [14,17] that is used to ensure

* Corresponding author.
E-mail addresses: armandoalfredo.escriba@urv.cat (A.A. Escriba-Flores), xavier.fernandez@upc.edu (X. Fernández-Francos), f.ferrando@urv.cat (F. Ferrando), a.fabregat@urv.cat (A. Fabregat-Sanjuan).

https://doi.org/10.1016/j.eurpolymj.2025.113878
Received 26 December 2024; Received in revised form 18 February 2025; Accepted 28 February 2025
Available online 2 March 2025

complete polymerization upon heating. Despite these advancements, both single and dual-stage curing systems face challenges during post-processing. They are optimized for parts with predetermined mechanical properties, but once solidified in the initial stage, altering geometries becomes difficult as the material is designed to achieve high mechanical performance [17].

The liquid state of the resin is also crucial for both processing and mechanical properties. Its physical characteristics depend on the formulation, particularly the molecular weight of the base material. Higher molecular weight resins generally exhibit superior mechanical properties [18,19] but also higher viscosity, leading to longer processing times and more complex setups. Conversely, lower viscosity resins, associated with lower molecular weights, enable faster processing but often result in brittle materials with reduced strengths and durability. Balancing molecular weight, processing time, and mechanical performance is key to optimizing resin formulations for various applications [13,20].

Another important challenge in this technology is the influence of material properties on large-scale production and the limited availability of 3D printers with large build volumes [21–23]. Printing large parts is challenging because they can suffer swelling or shrinkage, causing internal stresses or deformations that can create failures or defects in the printed parts [9,13].

The dual curing concept [24] enables the combination of 2 different polymerization processes, which are activated in a controlled and sequential manner, in a staged curing process. This makes it possible to generate hybrid materials formed by a co-network structure with good compatibility and interaction between both components [14,25–28], and with interesting intermediate and final mechanical properties from the point of view of their application [29,30]. On the other hand, the availability of different activation mechanisms allows the application of this concept to 3D printing, which allows exploiting 1) the ease of processing of complex geometries by 3D printing of photoactive resins and 2) the excellent mechanical properties of an epoxy resin. This combination presents interesting applications from the point of view of processability, and the characteristics of the materials obtained [29,30], which allows addressing the previously detailed challenges and evidencing a possible route to obtain new materials available for the industry. There exists potential for exploiting the flexibility of the intermediate material to produce complex geometries: simple initial shapes can be easily and quickly 3D-printed, followed by reshaping in a subsequent tooling process for the second curing stage [31]. This opens a way for the de-bottlenecking of production lines based on 3D-printing. Moreover, the presence of unreacted groups in the intermediate sate confers the printed parts interesting adhesion capabilities that can be used to produce larger components from printed parts [31] or in combination with other materials [30].

One particular dual-curing system for VAT 3D-printing applications was recently described in the literature, consisting in the combination of the radical homopolymerization of acrylates/methacrylates for the UV-activated 3D-printing stage, with the cationic ring-opening polymerization of epoxides activated using a thermally latent cationic initiator [32]. The reactions taking place in this dual-curing system are shown in Scheme 1.a (acrylate homopolymerization) and Scheme 1.b (epoxy ring-opening polymerization). An excellent control of the curing sequence and latency of the curing system was achieved and the formulations showed a good printing ability [32], but mechanical properties of the intermediate and final materials were neither studied in detail nor optimized. According to Scheme 1.a and Scheme 1.b, two different polymer networks would be present in the material structure: a poly (meth)acrylate network, and a polyether network, leading to an interpenetrated network-like structure. In analogous acrylate/epoxy dual-curing systems for VAT 3D-printing it was indeed observed that nano-structured topologies could be obtained, showing independent mechanical relaxations corresponding to the acrylate-rich and epoxy-rich phases [31,33]. The addition of a suitable coupling agent enabling

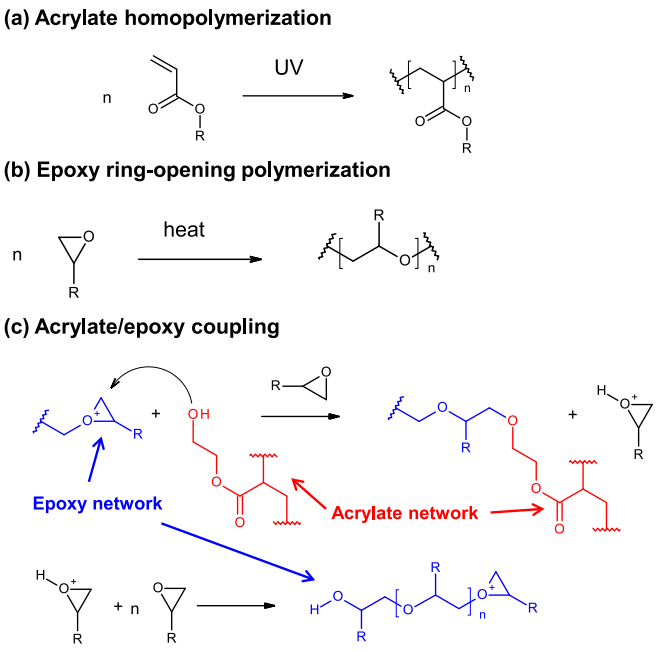

Scheme 1. Reactions taking place in the dual-curing process of the systems under study. (a) UV-activated radical acrylate homopolymerization (1st curing stage) (b) cationic ring-opening polymerization and (c) final configuration, bonding the acrylic and epoxy networking.

covalent interactions between the epoxy and acrylate networks would result in materials with a more uniform network topology showing a single mechanical relaxation [31]. Dual-curing systems are promising for 3D printing, offering enhanced mechanical properties, yet most studies focus on bulk materials and typically report tensile, compression, or flexural tests [34,35]. However, pure shear strength is often neglected, despite its importance for joint behavior and structural design. Additionally, intermediate-state properties are rarely explored, and many formulations exhibit high viscosities [20,34]. The mechanical performance of joint interfaces and adhesion also remain largely unaddressed, even though these factors are crucial for large-scale part assembly.

In the present work we want to take advantage of the excellent reactivity and latency of the acrylate/cationic epoxy system [32], to design dual-curing systems with controlled intermediate and final structure, having excellent compatibility between the epoxy and acrylate networks. Cationic ring-opening polymerization is known to proceed via the so-called active chain-end mechanism (ACE) and activated monomer mechanisms (AM) [36]. According to the AM mechanism, hydroxyl-bearing compounds would interact with the growing chains leading to a chain-transfer reaction and reinitiation of the active growing chain. It is proposed that the use of hydroxyl-containing acrylate components would facilitate the effective covalent interaction between the acrylate and epoxy networks, leading to a co-network structure, as indicated in Scheme 1.c: the pendant hydroxyl groups from the acrylate network would react with the growing epoxy polymer chain, leading to a covalent bonding between the acrylate and epoxy network, and a re-initiation of a new epoxy polymer chain. Moreover, the use of a mono methacrylates with pendant hydroxyl groups should also contribute to modify the structure of the acrylic network, making it possible to fine-tune the mechanical properties of both the intermediate and final materials. Moreover, it is also intended to exploit the possibilities of dual-curing systems with the purpose of creating complex shape specimens and joints making use of the dual-curing processing scheme with controlled intermediate material properties. For that purpose, a dual curing system that combines a commercial acrylic resin with a cycloaliphatic epoxy resin is analyzed. The system has been

conveniently modified with the incorporation of (meth)acrylates bearing hydroxyl groups. The UV-curing and thermal curing stages will be studied separately before transferring the formulations to the 3D-printer. Specimens for detailed mechanical and adhesion/reshaping have been printed and their performance have been tested under suitable scenarios. The effect of the coupling agent on the reactivity and the thermal–mechanical properties of the material have been studied in detail, as well as on other properties of interest such as the stability of the printing formulations and their processing ability.

2. Experimental part

2.1. Materials

Commercial acrylic resin Spot-E composed of mono- and di-(meth) acrylates groups provided from Spot-A Materials (Barcelona, Spain) was used as base acrylic component. Epoxy resin (3,4-Epoxycyclohexylmethyl 3,4-epoxycyclohexane carboxylate, 252.31 g/mol). 2-(Hydroxyethyl)methacrylate (HEMA, 130.10 g/mol), triethanolamine (TEA, 149.20 g/mol), propylene carbonate (PC, 102.10 g/mol) and photoinitiator 2,4,6-trimethylbenzoyldiphenyl phosphine oxide (TPO) were provided by Sigma-Aldrich (Schnelldorf, Germany). Radical thermal initiator 1,1-Bis(*tert*-amylperoxy)cyclohexane (Luperox 531 M60) was provided by Arkema (Günzburg, Germany). Cationic initiator K-PURE CXC-1612 was provided by King Industries (Norwalk, Connecticut, USA).

The schemes of the different components used for the preparation of the formulations, with the exception of the components in the proprietary Spot-E formulation, are shown in Scheme 2.

2.2. Formulation

Formulations were prepared containing different fractions of base acrylic resin Spot-E, epoxy resin, and HEMA as coupling agent. The formulations were coded as RACxACy, where x is the weight percentage (wt.%) of base acrylic resin, y is the wt.% of coupling agent, and the wt. % of epoxy resin is equal to 100-x-y. The different compositions are shown in Table 1. For all formulations, 2.70 wt% of TPO photoinitiator and 2 wt% of a cationic initiator solution were used.

The cationic initiator solution was prepared by dissolving 50 wt% of CXC-1612 and 5 wt% of TEA in PC (up to 100 wt%) with the help of a magnetic stirrer.

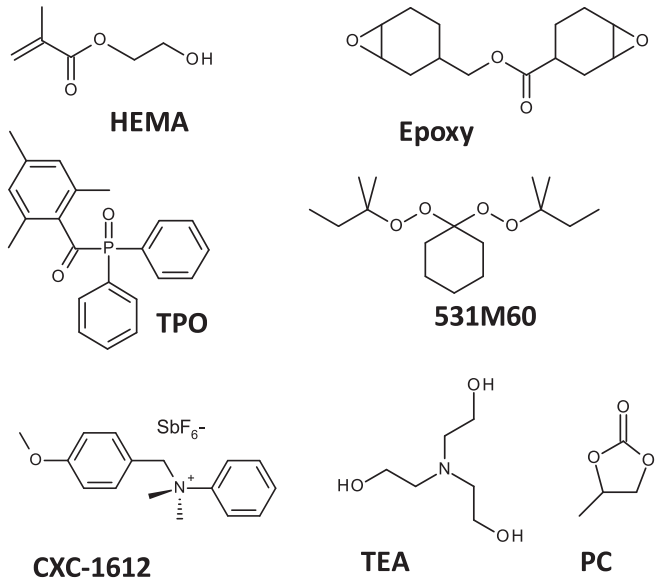

Scheme 2. Components used for the preparation of the dual-curing formulations shown in this work, with the exception of the methacrylic components of the proprietary Spot-E formulation.

Table 1
Composition and notation of the different formulations used in this work. Weight percentages shown in the table exclude the different initiators used.

Formulation	Acrylic base (wt.%)	HEMA (wt.%)	Epoxy (wt.%)
RAC100AC0	100	0	0
RAC20AC5	20	5	75
RAC20AC20	20	20	60
RAC20AC30	20	30	50
RAC20AC40	20	40	40
RAC20AC50	20	50	30

Formulations were prepared by mixing the different components in a glass vial or bottle and homogenizing with a magnetic stirrer. The formulations were allowed to rest for at least 10 min before preparing the samples for UV-flood curing or printing.

2.3. Preparation of samples

Samples for thermal analysis testing were prepared by UV flood curing in a Vilber Lourmat crosslinker (Marne-la-Vallée, France) equipped with 360 nm lamps with an average intensity of 4 mW/cm^2. A prismatic rectangular mold prepared using a 1 mm thick Teflon spacer and 0.50 mm thick transparent polypropylene on both sides, was filled with the liquid formulations using a syringe. The samples were irradiated on both sides for 5 min leading to the intermediate UV-cured material. Fully cured material specimens were prepared by keeping the samples in a thermal oven 3 h at 150 °C in order to ensure complete reaction of epoxy groups.

2.4. 3D printing processing and, UV and thermal treatment

3D-printed samples were prepared in an ASIGA MAX-UV 3D printer (Sydney, Australia) with a 385 nm lamp, an intensity of 4.77 mW/cm^2 and a layer thickness of 0.07 mm. In order to determine the optimal exposure time, Jacobs working curve of each formulation were prepared. Three samples of each formulation underwent radiation at an intensity of 4.77 mW/cm^2, utilizing a wavelength of 385 nm (on the ASIGA-MAX-UV 3D printer) with an exposure duration ranged from 10 to 60 s within a circular section measuring 10 mm in diameter. The thickness or curing depth (Cd) was subsequently measured using a micrometer. For each formulation, a straight line was plotted on a logarithmic scale. The behavior of the curve was modeled by the following equation:

$$C_d = D_p Ln\left(\frac{E}{E_c}\right) \quad (1)$$

Here, C_d (μm) represents the cure depth/thickness of the sample, E_c is the critical energy and E the maximum energy (mJ·cm^{-2}) of the incident light on the surface, and D_p (μm) is the penetration depth of the light. When C_d is plotted against E on semilogarithmic axes, a straight line should be obtained by linear regression of the different datapoints. E_c can be determined from the intersection with the x-axis, while D_p is calculated from its slope.

The printed samples were rinsed in isopropyl alcohol and exposed to a UV post-curing process within a DentalFarm Photopol (Pordenone, Italy) oven under vacuum (−0.09 MPa) and an intensity of 200 W in order to obtain partially cured specimens with fully reacted acrylate groups. Completely cured specimens were prepared by keeping the printed samples for 3-hours at 150 °C in a conventional oven in order to ensure complete reaction of all the epoxy groups.

2.5. Thermal characterization

To analyze the kinetics of the first stage of curing, the photocurable solution was placed in a customized Mettler DSC 821e calorimeter (Greifensee, Switzerland), equipped with a Hamamatsu Lightning cure LC5 (mid-pressure Hg-Xe lamp) (Hamamatsu, Japan) with two light-guides —one for the sample side and the other for the reference side. Approximately 2 mg were placed in open aluminum pans within in nitrogen atmosphere. Samples were kept at 30 °C for 2 min before exposure, irradiated for 8 min at 30 °C with a light intensity of 20 mW/cm^2, followed by 2 more minutes with the light off. Experiments were carried out under nitrogen atmosphere (50 ml/min). In order to account for the thermal influence of UV irradiation during the photocuring experiment, two consecutive runs were performed on each sample; the second run was substracted from the first run in order to obtain the rate of polymerization and reaction heat.

The kinetics of the second curing stage were determined by DSC (Differential Scanning Calorimetry) using a Mettler DSC3+ (Greifensee, Switzerland) equipped with an intra-cooler. Samples from 3 to 15 mg in weight were placed in pierced aluminum pans and analyzed from −50 °C to 250 °C in nitrogen atmosphere (50 ml/min) at heating rates of 1.25, 2.5, 5, 10 and 20 °C/min. The apparent activation energy was determined using the Starink isoconversional integral method [28,37]. This information was used to make isothermal curing predictions. All the details about the kinetics analysis and predictions methodology can be found in the Supporting Information.

The thermal stability of the materials was determined using a Mettler TGA/DSC (Greifensee, Switzerland). Samples of 15 mg were analyzed in silica crucibles under nitrogen atmosphere (50 ml/min) from 25 to 800 °C at a heating rate of 10 °C/min.

Samples were analyzed using a dynamomechanical analyzer TA Instruments DMA Q800 (New Castle, Delaware, USA). Samples with dimensions 10x5x0.5 mm were analyzed in single cantilever mode with an oscillation strain of 0.10 %, heated at 3 °C/min from 25 to 200 °C, in dry air atmosphere. The glass transition temperatures of the materials were determined as the tan δ peak of the α-relaxation.

A Brucker Vertex 70 FTIR spectrometer (Billerica, Massachusetts, USA) equipped with an attenuated total reflection (ATR) accessory (GoldenGateTM by Specac Ltd.) (Orpington, United Kingdom) was used to determine the infrared spectra of uncured, partially cured and fully cured materials. Samples were analyzed from 4000 cm^{-1} to 600 cm^{-1} with a resolution of 4 cm^{-1}. 20 scans were averaged for each spectrum.

2.6. Viscosity measurements

The viscosity was measured with an IKA ROTAVISC me-vi viscometer (Staufen im Breisgau, Germany), equipped with a low-volume measurement cell (VOL-SP-6.7) temperature-controlled with the help of an external thermostated bath. Approximately 7 cc of solution was placed inside the container. Dynamic viscosity (mPa·s) was measured at 30 °C and rotational speed of 11.2, 33.6, 56, 112, and 224 1/s. The viscosity as a function of shear rate was measured using a TA Instruments HR20 rheometer (New Castle, DE, USA) in a plate-plate configuration. Disposable aluminum plates (25 mm diameter) were used to prevent cross-contamination between measurements. The tests were conducted at 30 °C, controlled by an electrical heating plate (EHP) system, with shear rates ranging from 0.10 to 3000 s^{-1}.

2.7. Mechanical characterization

The test specimens were prepared in accordance with ISO 527–2, Type 5B geometry. Mechanical testing was carried out using a Shimadzu AGS-X-10 kN universal testing machine (Kyoto, Japan), equipped with a 500 N load cell, at a constant crosshead speed of 1.5 mm/min. Both partially cured and fully cured 3D-printed specimens were tested. Five specimens were analyzed for each curing state and formulation to ensure statistical relevance.

The strength of mechanical joints produced exploiting the dual-curing concept, as outlined in the literature [31], was analyzed in detail. For that purpose, 3D-printed parts were joined by (i) applying uncured liquid formulation on the surfaces to be joined, (ii) physical assembly of the parts to be joined, (iii) UV-curing of the joint by exposure and (iv) thermal curing of the joined parts in order to obtain fully cured materials. The joint strength was analyzed in two scenarios: tensile and shear. The different geometries and procedures are illustrated in Fig. 1. Tensile tests used specimens with dimensions as per ISO 527–2, Type 5A, with a thickness of 2.5 mm. For shear tests, a prism measuring 1.5x3x3 mm was employed. Such detailed analysis was only performed for the formulation RAC20AC40 and compared with the results obtained using bulk 3D-printed samples. Given the higher level of experimental uncertainty introduced by the preparation of the joint, 8 joined samples were analyzed for each scenario.

The analysis of bonding through lap-shear testing is a widely recognized method that provides comparative information on the shear mechanical properties of adhesives. This test not only evaluates the adhesive's performance in relation to the selected adherend but also categorizes the type of failure based on the adhesive and adherend behavior. The lap-shear test involves using two rectangular elements that overlap in a central zone where the adhesive is applied. These elements are then subjected to tension, inducing shear stresses in the adhesive. However, one of the main limitations of this method is the bending moments generated in the adherends due to system eccentricities, which depend on the length of the free adherend without overlap [38,39]. These stresses can cause the adherends to fail before the adhesive. Therefore, it is crucial to control the overlap area and understand the mechanical properties of the adherend to prevent premature failure [40].

The ISO 4587 standard specifies the dimensions of the specimens for performing lap-shear adhesive tests, indicating that the overlap area must be significantly larger than the cross-sectional area of the adherends. This difference in areas implies that the mechanical properties of the adherend must be greater than those of the adhesive. This approach makes it unfeasible to use the same material for both the adherend and the adhesive, as the disparity between the overlap area and the cross-sectional area of the adherend induces a bending moment in the adherend, leading to its failure. To address this issue, a specialized tooling has been developed. Fig. 1.b shows the tooling used to analyze direct shear. This tooling allows for a more accurate assessment of adhesive performance, eliminating the complications associated with traditional lap-shear testing. The tooling uses a 0.01 mm gap in the shear zone. This value is constant while the test is performed thanks to the geometry of the tooling and the symmetry of forces generated. In contrary to the lap shear, with this tooling the bending forces are counteracted. More details on the tooling can be found in the Supplementary Information.

3. Results and discussion

3.1. Kinetics analysis of the dual-curing process

First of all, the reaction kinetics of the two curing stages was analyzed. In Fig. 2 we represent two thermograms corresponding to the isothermal photo-DSC analysis of the 1st curing stage (a) and the non-isothermal DSC analysis of the 2nd curing stage (b) of the RAC20AC20 formulation. As seen in Fig. 2.a, the photocuring process is fast, as expected, completing in about 1 min once the irradiation is started and the photoinitiator is activated leading to the release of the radical initiating species. The analysis of the 2nd curing stage in Fig. 2.b shows that the reaction starts once the sample is heated above 100 °C, evidencing the high latency of the cationic process. This was to be expected, taking into consideration the preceding results [32], despite the modification of the system by means of the HEMA coupling agent.

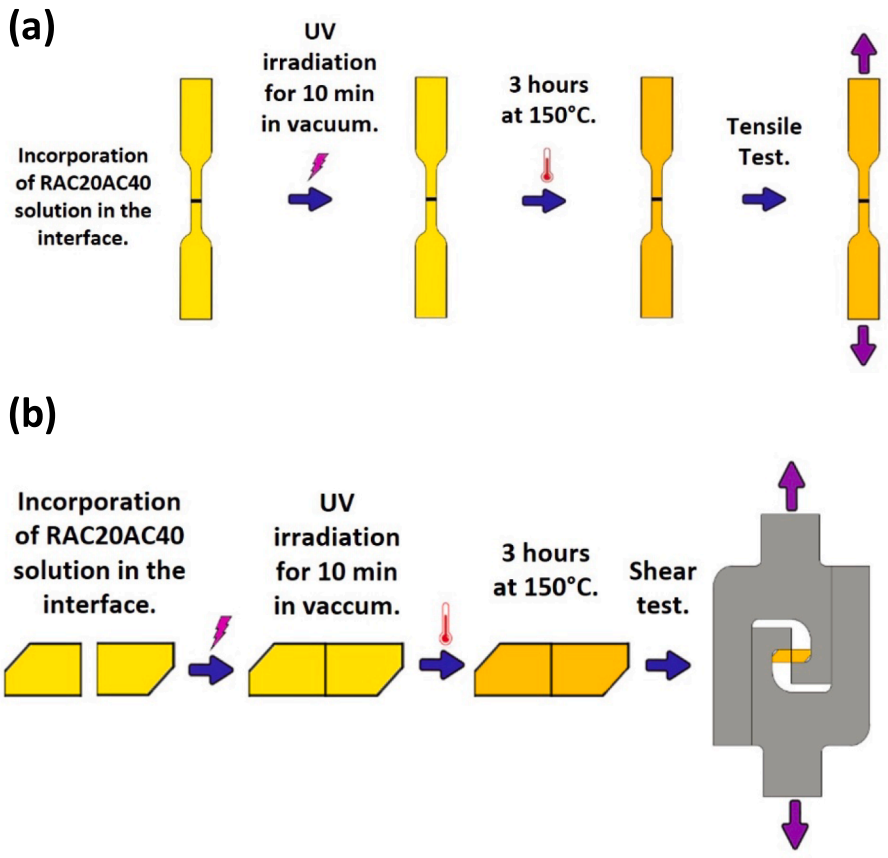

Fig. 1. Representative scheme for the preparation of joints and their mechanical analysis: (a) joints for tensile testing, (b) joints for direct-shear test using a tool developed in this work (the same tooling was used for the analysis of bulk samples).

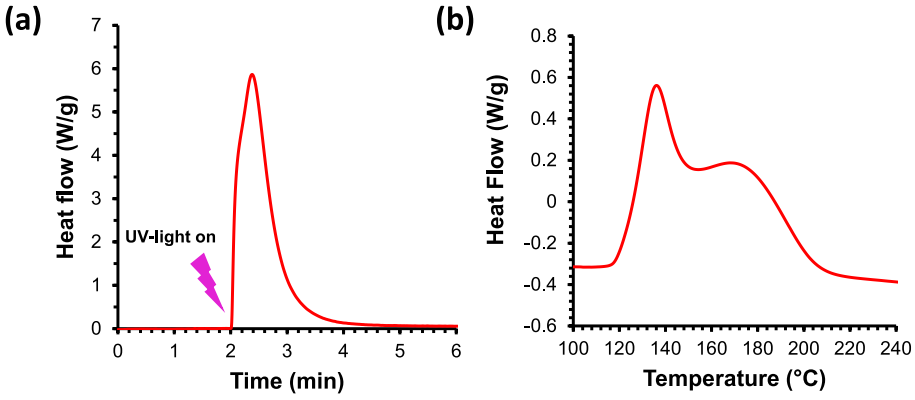

Fig. 2. DSC thermograms of (a) the isothermal photocuring process at 30 °C corresponding to the first curing stage of formulation RAC20AC40 (b) a dynamic postcuring at 10 °C/min after photocuring.

In the thermograms shown in Fig. S1 corresponding to the 2nd curing stage of the different formulations, it can be observed that increasing the coupling agent, which reduces the epoxy content, results in smaller exothermic peaks in the second curing stage. The heat released in both curing stages, as shown in Table 2, is consistent with the composition in the formulations shown in Table 1, as expected taking into consideration preceding results [32]. The reaction heat is consistent with the reaction heat observed for the cationic curing of cycloaliphatic epoxides, of approximately 80–85 kJ/mol [41,42]. Noteworthy, the curing kinetics of the different formulations is little affected by the changes in composition (see Fig. S1 in Supporting Information), showing similar latency, the reaction starting around 120 °C in all cases.

Table 2
Heat released in the 1st and 2nd curing stage for all the formulations.

Formulation	$\Delta h_1 (J/g)$	$\Delta h_2 (J/g)$	$\Delta h_{total} (J/g)$
RAC100AC0	311.27 ± 2.96	–-	311.27 ± 2.96
RAC20AC5	102.36 ± 0.86	438.10 ± 1.12	540.46 ± 1.41
RAC20AC20	168.66 ± 1.70	350.64 ± 0.52	519.30 ± 1.77
RAC20AC30	180.38 ± 1.24	302.85 ± 2.28	483.23 ± 2.60
RAC20AC40	252.36 ± 2.53	237.87 ± 0.28	490.23 ± 2.54
RAC20AC50	359.50 ± 0.52	193.98 ± 0.19	553.48 ± 0.56

The kinetics of the 2nd curing stage of RAC20AC40 formulation were studied in detail, making use of non-isothermal kinetic data collected at different heating rates, as seen in Fig. 3.a and Fig. S2 (see Supplementary Information). The kinetics analysis reveals that the second curing stage has a rather simple temperature dependence, given by the nearly constant apparent activation energy (see Fig. 3.b), which evidences that the curing process is simple (i.e. the epoxy homopolymerization via the AM and ACE mechanisms) and there are no major side reactions. Moreover, this kinetic information was used to make predictions of curing time at different isothermal temperatures (see Supplementary Information for the details on the methodology). In Fig. 3.c it can be observed that the 2nd curing stage proceeds quite fast at 150 °C, reaching 95 % conversion in about 1 h. In contrast, at 100 °C the reaction onset (5 % conversion) is delayed to around 20 min, which is an evidence of the latent character of the catalytic system. Noteworthy, it was attempted to extrapolate the reactivity to 30 °C, and it was observed that the reaction onset was delayed up to 82,000 min or, equivalently, 57 days. Even though such an extrapolation to a temperature clearly outside the experimental range (see Fig. 3.a) can induce quantitative errors, it is nevertheless a reasonable order-of-magnitude approximation [43], which reflects the high latency of this 2nd reaction and therefore the ability of these formulations to be safely stored for prolonged periods in the range of several weeks and the possibility of defining perfectly controlled curing sequences, as observed in previous works [32].

The FTIR analysis of the initial, intermediate and final materials also evidenced the good control of the curing sequence. Fig. 4 presents the infrared spectrum of the RAC20AC40 formulation. When comparing the spectra of the uncured liquid and the partially cured, full reaction of (meth)acrylate groups is evident from the disappearance of absorption bands between 800—820 cm^{-1}, 1295—1315, 1408—1415 cm^{-1}, and 1630 and 1640 cm^{-1} [44,45]. The presence of epoxy groups is made evident by the absorption bands at 780—790 cm^{-1} [46], vanishing after the second curing stage. Quantification is difficult, though, due to the small size of the peak and the presence of overlapping bands. Indirect confirmation of the complete reaction of epoxy groups was obtained from the reaction heat, as seen above. This observation strongly suggests the completion of the reaction involving the formation of new bonds through the reactivity of both the acrylic and epoxy in the first and second stage of curing respectably. As a result, the band in the IR-spectra corroborates other findings in the existing literature [31,47].

3.2. Thermomechanical analysis

The DMA analysis of the different materials evidenced strong differences in network structure with changing composition. In Fig. 5.a it can be observed that, when the content in HEMA coupling agent is the lowest and the epoxy content is the highest (RAC20AC5 formulation), the α-relaxation of the material, given by the tan δ peak, takes place at very high temperature, and is very broad and low. All these factors are indicative of a highly crosslinked and heterogeneous network structure, mainly due to the contribution of the cycloaliphatic epoxy homopolymer network, as commonly reported in the literature [42]. Given that the DMA experiments were carried out above room temperature, it was not determined whether a relaxation from the acrylic network or not was present, unlike other hybrid systems in which the same acrylic base formulation was used [31], having tan δ peak below room temperature. It could be that the relaxation could not be observed due to the reduced fraction of acrylic network. However, the value of tan δ peak temperature of the main relaxation, about 200 °C, is lower than the pure cycloaliphatic epoxy homopolymer network [42], suggesting there is already some compatibility between the acrylate and epoxy networks with little coupling agent present. Upon increasing the content in HEMA coupling agent and reducing epoxy content, the tan δ peak shifts to lower temperatures and becomes narrower and higher. All these factors evidence the formation of a lesser crosslinked and more homogeneous network structure. This is consequence of the participation of the hydroxyl groups of the HEMA present in the acrylic network structure (see Scheme 1), which become covalently bonded to the epoxy network epoxy, stopping chain growth and leading to formation of new chain starts, thereby increasing the homogeneity of the network structure and reducing the crosslinking density. Similar trends are observed in the evolution of the storage moduli E' (Fig. 5.b) and loss moduli E" (Fig. 5.c). In any case, the relaxation takes place at sufficiently high temperature so that the materials will behave as rigid glassy materials at room temperature [64,65].

Further characterization of the cured materials by TGA (see Fig. S3 in Supporting Information) illustrates the thermal degradation behavior of the fully cured formulations. Notably, all the materials exhibit robust thermal stability up to around 300 °C. Beyond this temperature, a unique stage of thermal degradation becomes apparent throughout the system. Interestingly, these findings align with those reported in existing literature for certain epoxy resins [48,49], consisting of bonds formed by both acrylic and epoxy groups. The existence of a single degradation process suggests there is a rather uniform network structure. The elevated thermal stability of the materials evidences the validity of the proposed curing schedule for the thermal curing stage, 3 h at 150 °C, which should not produce any unwanted degradation on the materials during processing.

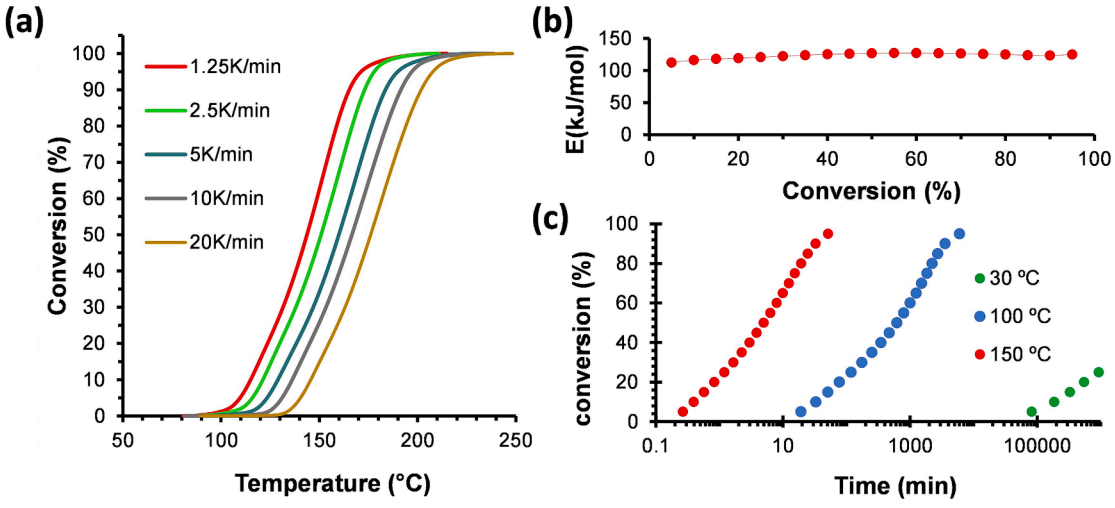

Fig. 3. Kinetics analysis of the 2nd curing stage of RAC20AC40 formulation. (a) conversion curves at different heating rates, (b) apparent activation energy obtained from the Starink method and (b) isothermal predictions made from the isoconversional data.

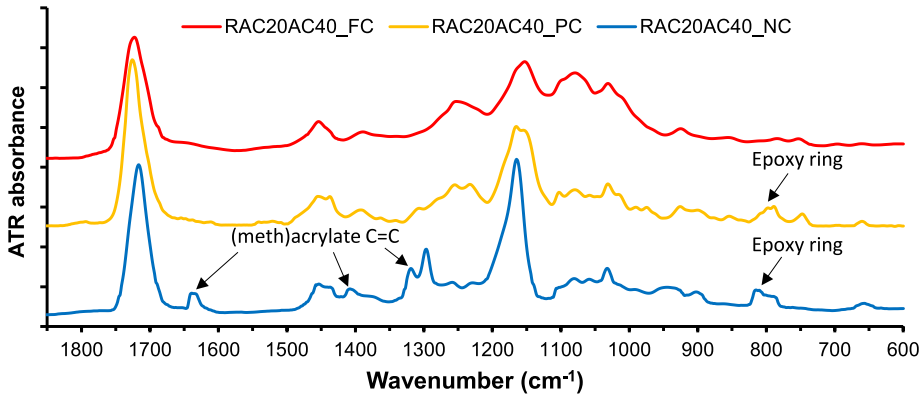

Fig. 4. FTIR spectra of the uncured (NC), partially cured (PC) and fully cured (FC) materials of RAC20AC40 formulation.

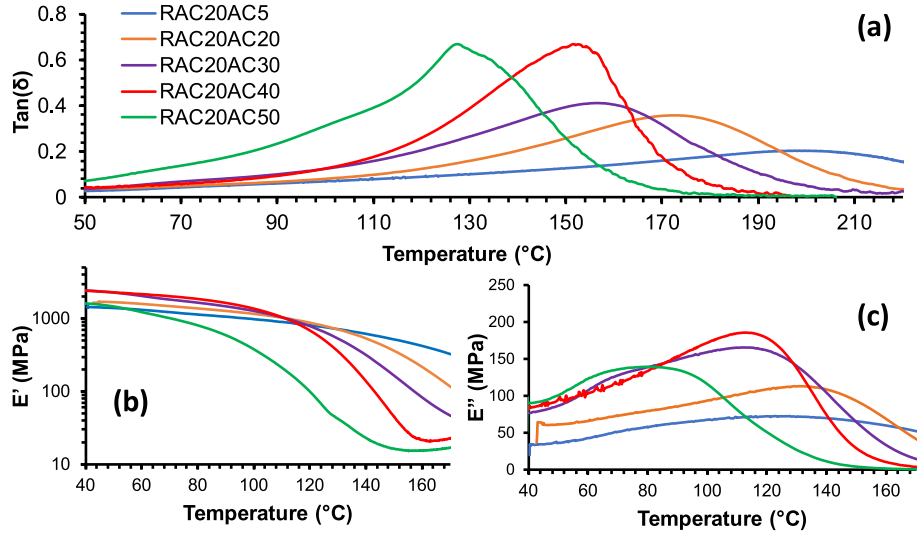

Fig. 5. Results of the DMA analysis of the final materials: (a) loss factor tan δ, (b) storage modulus E' and (c) loss modulus E''.

3.3. 3D-printing capabilities

To determine the printing ability of the materials, their viscosity was analyzed. Viscosity in 3D printing, frequently significantly influences both the ease of processing a material and its final practical application. Lower viscosity improves processing capabilities but often show low mechanical performance and are present such as brittle and not flexible materials [50,51]. Conversely, high viscosity is associated with better mechanical performance but affects processing, as it is time-consuming and does not flow properly onto the platform, limiting both efficiency and print quality [19]. Fig. 6.a shows that the viscosity of the epoxy resin is higher than the starting acrylic formulation. It should come as no surprise that mixtures from the acrylic and epoxy components would have a higher viscosity than the acrylic resins. However, the presence of

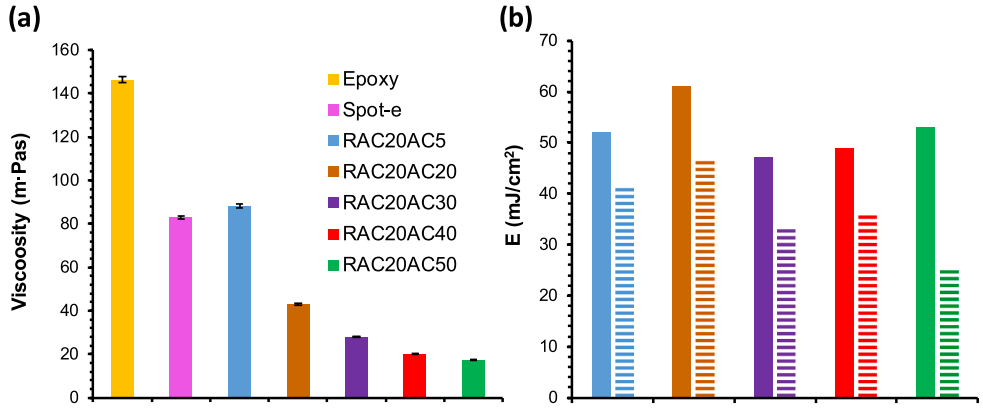

Fig. 6. (a) Viscosity of the different formulations measured in the rotary viscosimeter at 50 rpm and (b) energy dose required for a layer thickness of 70 μm (solid bar) and critical energy dose for the formation of a solid layer (patterned bar), determined from the Jacob's curves of the different formulations (see Supporting Information Fig. S4).

the low viscosity HEMA coupling agent should mitigate this effect. Indeed, formulation RAC20AC5 has a viscosity only slightly higher than the starting acrylic component. Moreover, upon further increasing the content in HEMA and reducing the epoxy content, the viscosity of the formulations drops to values lower than 20 mPa·s for the RAC20AC50 formulation. This reduction proves advantageous, streamlining the processing procedures within the vat photopolymerization 3D printer.

Fig. S4 (a to e) shows the Jacobs working curve for all the formulations. Examining the energy trend in relation to the quantity of HEMA bonding agent and viscosity reveals interesting insights. Despite the similarities in values, a notable pattern is evident when the viscosity decreases due to the introduction of the HEMA there's a corresponding decrease in the critical energy. This phenomenon becomes clear because, at this stage, the reactive phase within the network is improved as increase the percentage of HEMA, making the formation of a layer more efficient. Additionally, the curing times for producing thin layers of 0.07 mm are relatively short, around 20–25 s. These optimized conditions yield layers with favorable mechanical properties without compromising the geometric integrity of the part. This analysis underscores the potential to manufacture components with intricate geometries. The process is efficient, demonstrating the ability to produce such parts in relatively brief timeframes. In Fig. S4-c, an analysis of the Cd graph is presented for each of the solutions, using a constant dose of 35 s at 4.77 MW/cm^2. Since the Cd value is associated with the thickness of a cured layer, the values shown in the graph demonstrate a tendency to decrease as the concentration of HEMA in the system increases. Although the changes are very subtle for the formulations RAC20AC5, RAC20AC20, RAC20AC30, and RAC20AC40, they are very evident for the formulation RAC20AC50. This phenomenon can be attributed to the fact that HEMA occupies more space in the system and, being a methacrylate, does not react as quickly as the acrylic groups present in the resin.

Therefore, the use of HEMA coupling agent plays a complex role in processing: on one hand, the decrease in viscosity evidences an improvement in the flowability of the material within the manufacturing process; on the other hand, Cd values remain relatively constant around 310 μm but decrease to approximately 160 μm for solution RAC20AC50, indicating longer curing times for layer formation. The printing behavior could be tuned by adjusting the initiator content and using printing inks to control resolution

Fig. S5 presents a collection of images exposing the printing resolution and ductile characteristics of the RAC20AC40 formulation in its partially cured state. The visual representation underscores the adaptability of the printed components, demonstrating the capacity to effectuate diverse geometric modifications. This dual-system approach facilitates uniform adoption of these novel printed forms, transitioning effortlessly from a ductile to a rigid material while maintaining a high mechanical resistance. Furthermore, the versatility of the printed parts is exemplified through an examination of complex joint formations capable of withstanding substantial structural loads. The figures illustrate the creation of T-type joints, serving as a conceptual demonstration of the formulation's potential to generate intricate connections. This empirical evidence reinforces the formulation's applicability in engineering contexts where mechanical strength and adaptability are paramount considerations.

Fig. S6 illustrates the apparent viscosity as a function of shear rate, confirming a predominantly Newtonian behavior, with viscosity remaining nearly constant across the tested shear rate range. The formulations exhibited low viscosity, and no significant differences in printing resolution were observed. This is further indicated in Fig. S7, which provides a comparative analysis of the commercial Spot-E resin and the formulations RAC20AC5 and RAC20AC50.

3.4. Mechanical analysis

The intermediate, partially cured materials obtained after the UV-activated reaction of (meth)acrylate groups show diverse mechanical properties due to the contribution of HEMA and the presence of unreacted epoxy monomers, having a strong impact on the maximum tensile stress, modulus of elasticity, and strain. Fig. 7.a shows tensile-strain curves for all the formulations in the intermediate cured state. Fig. 7.b summarizes the effect of HEMA on the elastic modulus, and Fig. 7.c shows the effect on the strain at break.

As seen in Fig. 7, the starting Spot-E material has a remarkable stress and stress at break and elastic modulus. However, upon addition of a small amount of coupling agent and a large fraction of epoxy monomer (formulation RAC20AC5) the properties decrease considerably. The presence of the unreacted epoxy monomer leads to a swollen acrylate network structure which is softer (i.e. lower modulus) due to the reduced concentration of acrylate crosslinks in the network structure. For that same reason, the network chains in this swollen polymer network are already stretched and will not withstand excessive additional mechanical strain, therefore leading to a significant decrease in the stress and strain at break. However, increasing the HEMA content and reducing epoxy content lead to acrylate networks which have higher stretching ability (due to the role of HEMA as chain extender), and a lower degree of swelling (due to the lower epoxy content, which reduces the level of stretching of the acrylate network chains and therefore increases mechanical stretching capabilities of the material, producing an increase in the stress and strain at break. In fact, a maximum strain at break is reached with 30 wt% of coupling agent and 50 wt% of epoxy content (RAC20AC30), reaching values up to 160 %, but the best combination of mechanical strength (elastic modulus, stress/strain at break) is obtained with 50 wt% of coupling agent and 30 % epoxy content (RAC20AC50), reaching stress and strain at break of up to 12 MPa and 130 %. An additional strengthening effect may be caused by the presence of HEMA, which increases the methacrylate content of the acrylic network therefore increasing modulus and Tg (as reported in the literature [52], Poly(HEMA) inherently represents a rigid polymer with a Tg exceeding 90 °C); in addition, the OH groups from HEMA can also contribute to the mechanical strength of the materials due to the additional contribution of hydrogen bonding. this trend is associated with the hydrogen bonds that allows high deformation.

It is therefore quite apparent that a successful design of dual-curing system with intermediate mechanical strength and stretching ability depends on a suitable combination of both chain extender (which will also act as coupling agent) and epoxy component in the formulation, in order to make up for the detrimental swelling effect of the added epoxy component. To the best of our knowledge, such considerations were neglected in preliminary studies about acrylate-epoxy sequential dual-curing systems for 3D-printing applications [32,33,53,54], focusing mainly on the control of the curing sequence and the effect on the final mechanical properties.

On the other hand, when analyzing the fully cured specimens, a rigid behavior is observed in all the formulations, which could be expected taking into consideration that the final materials have an elevated Tg significantly above room temperature. Fig. 8.a shows stress–strain chart, Fig. 8.b shows the Young modulus and Fig. 8.c shows the HEMA-Strain (%) chart for all the formulations. No drastic changes were observed across the various formulations in terms of max tensile stress, young modulus, and strain. Nor were significant changes observed in the strain in the partially cured state. This suggests that there is no apparent negative impact within the system, even with a low percentage of epoxy resin participation.

To conduct the shear stress test, a custom tool developed for this study was utilized, employing the shear stress condition (tool used describe in Fig. 1 (B)). The obtained results from this test indicated that the samples, when fully cured bulk, exhibited shear stress values above 50 % of the tensile test. Fig. 9.a shows the mechanical behavior of the pieces subjected to shear stress, revealing that the formulations exhibit significant rigidity with values ranging from 40 to 60 MPa. Fig. 9.b illustrates the shear modulus of all formulations, which display a uniform

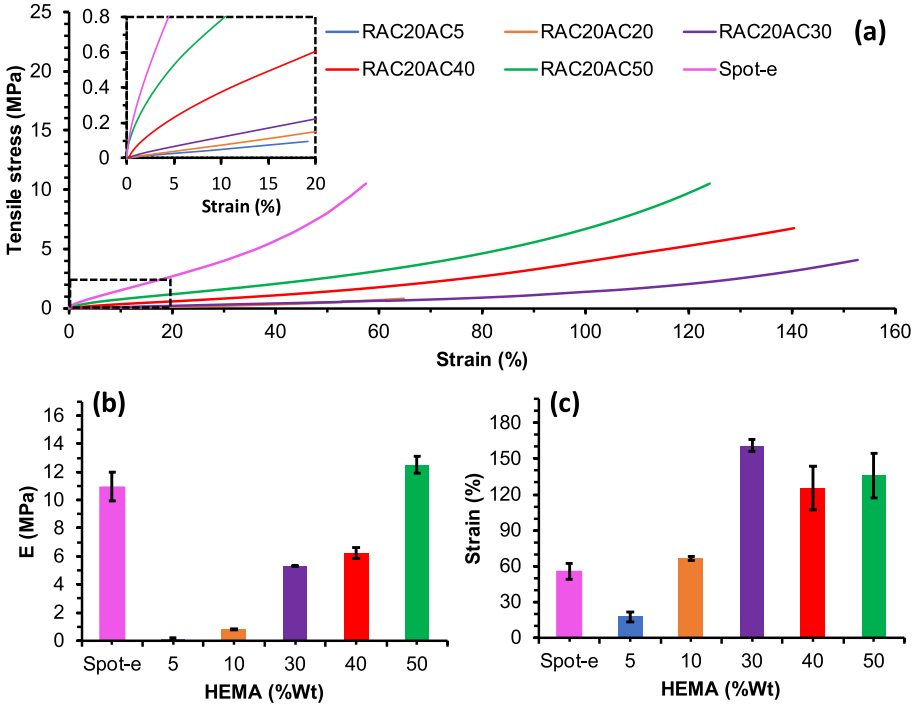

Fig. 7. Stress–strain charts from partial cured state (a) Tensile stress (MPa) – Strain (%), (b) Young modulus (MPa) – HEMA (%wt) chart and (c) Strain (%) – HEMA (%wt) chart.

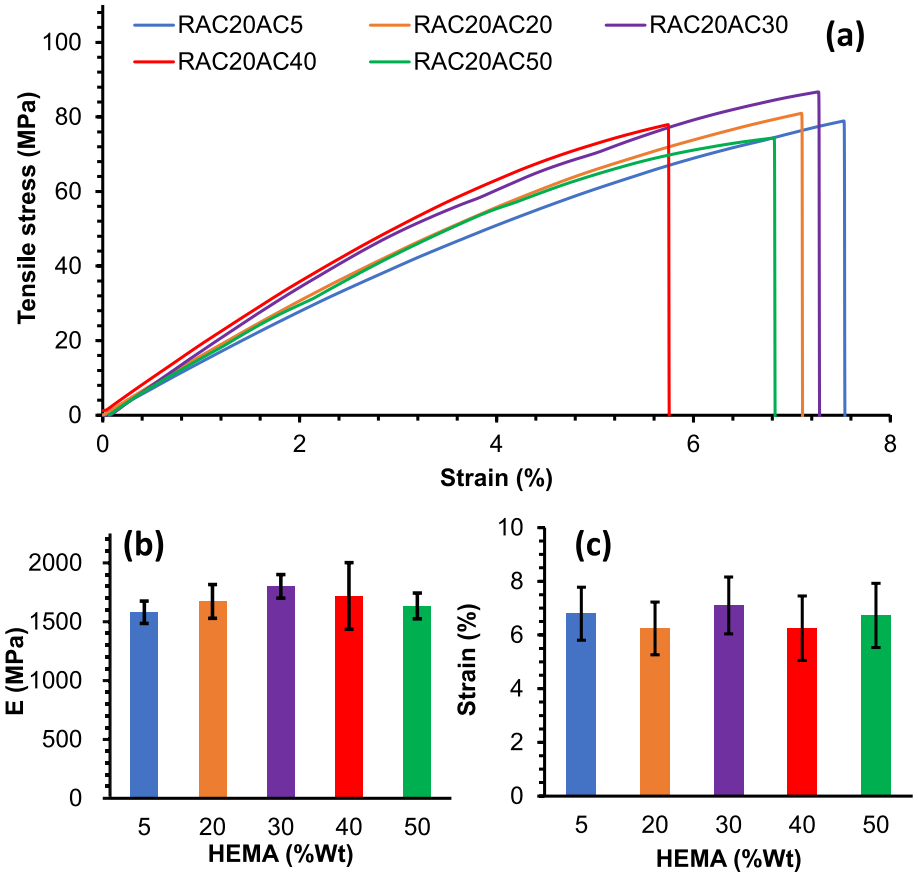

Fig. 8. Stress–strain charts from totally cured state (a) Tensile stress (MPa) – Strain (%), (b) Young modulus (MPa) – HEMA (%wt) chart and (c) Strain (%) – HEMA (%wt) chart.

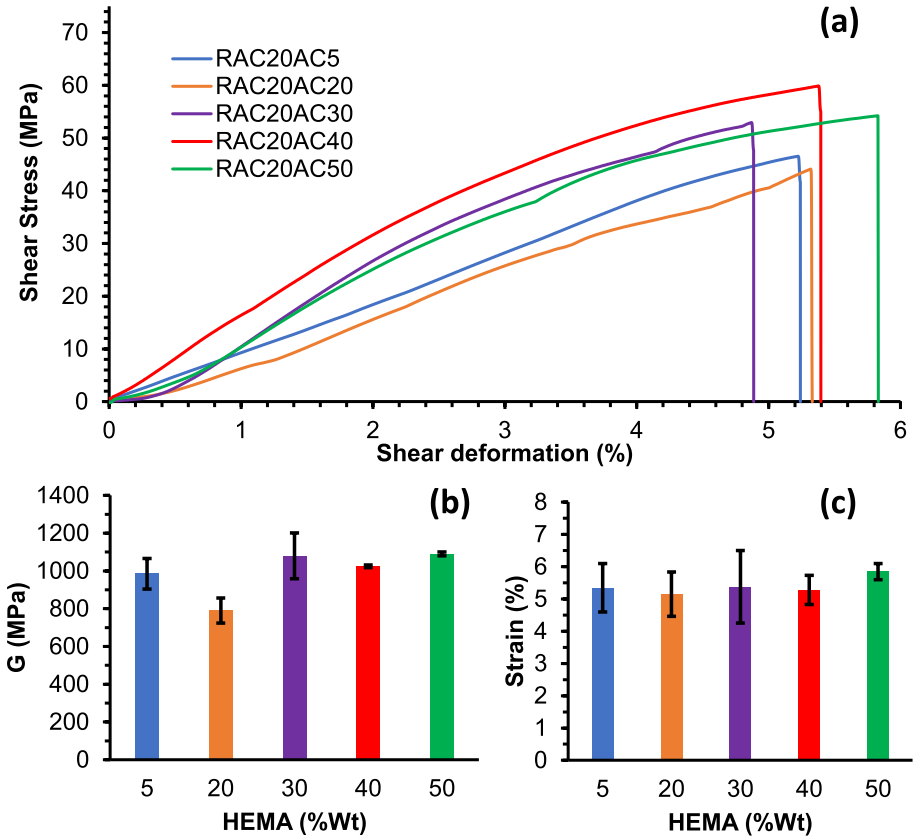

Fig. 9. (a) Shear Stress-Strain chart from totally cured state (b) Shear modulus (G) – HEMA (%wt) chart, and (c) Strain (%) – HEMA (%wt) chart.

behavior with values between 800 and 1000 MPa. On the other hand, shear strain values range between values of 5 and 6.5 %, as seen in Fig. 9. c.

Table 3 provides a comprehensive summary of the mechanical, thermal, and processing properties for each of the solutions under study. The crucial role of hydroxyethyl methacrylate (HEMA) in the mechanical properties in the intermediate state is highlighted, where a significant increase in all variables is observed, suggesting a significant constructive contribution. Particularly notable is the increase in strain, tensile strength, and elasticity modulus, which exceed 150 %, more than 12 MPa, and 5 MPa respectively. This phenomenon suggests that there is an effective modification of the original acrylic matrix with HEMA, having a positive impact on the mechanical responses of the partially cured materials. Similarly, when analyzing the mechanical properties in the fully cured state, subtle variations in tensile strength are observed, with maximum values close to 82 MPa for solution RAC20AC30 and minimum of 68 MPa for solution RAC20AC5. These discrepancies evidence the changes in the mechanical properties of the materials once they have completed the curing process due to the varying contribution of the epoxy matrix and the coupling agent, leading to different network architectures, as discussed before in the DMA analysis of the cured materials.

On the other hand, the analysis of the joints demonstrated excellent adhesion between the phases of the RAC20AC40 formulation. The tensile test results for the joints showed an impressive 64.72 ± 11.34 MPa, which is very close to the values achieved by this formulation in bulk, measured at 73.62 ± 6.12 MPa. This represents approximately 87 % of the bulk tensile strength on average. Additionally, the values for the joined pieces under shear stress exhibited a maximum shear strength of 34.53 ± 6.56 MPa, compared to a bulk value of 54.90 ± 5.95 MPa, which corresponds to about 62 % of the bulk shear strength, indicating a respectable performance. The direct shear stress in the joints can be compared to the results found in lab shear tests and direct shear tests in commercial resins, FDM additive manufacturing polymers, where it is rare to achieve values exceeding 30 MPa [55–57]. This indicates that the RAC20AC40 formulation surpasses many of the materials reported in

Table 3
Summary of principal mechanical, thermomechanical and processing properties.

Area	Property	RAC20AC5	RAC20AC20	RAC20AC30	RAC20AC40	RAC20AC50
Mechanical	Max tensile stress (UV), MPa	0.10 ± 0.02	0.83 ± 0.01	5.30 ± 1.33	6.25 ± 0.57	12.51 ± 2.48
	E (UV), MPa	0.59 ± 0.07	0.81 ± 0.01	1.10 ± 0.02	2.36 ± 0.40	4.52 ± 0.62
	Strain (UV), %	17.36 ± 3.80	66.65 ± 1.68	161.05 ± 4.86	125.07 ± 18.24	135.91 ± 18.87
	Max tensile stress (UV-CC), MPa	68.40 ± 12.70	72.70 ± 10.30	81.20 ± 7.20	73.62 ± 6.12	69.80 ± 5.90
	E (UV-CC), MPa	1580.01 ± 94.35	1672.70 ± 143.33	1800.12 ± 100.61	1728.25 ± 274.02	1633.40 ± 109.73
	Strain (UV-CC), %	5.80 ± 1.66	6.23 ± 0.98	7.01 ± 1.06	5.06 ± 1.52	6.72 ± 1.19
	Max Shear stress (UV-CC), MPa	54.31 ± 7.74	37.60 ± 5.58	57.86 ± 4.98	54.90 ± 5.95	47.26 ± 8.58
Thermo-mechanical	Max Tan delta (UV-CC)	200 ± 1	173 ± 1	156 ± 1	152 ± 1	127 ± 1
	E' 60 °C (UV-CC), MPa	1319.12 ± 7.74	1585.18 ± 3.46	2038.57 ± 7.83	2191.24 ± 7.20	1210.35 ± 1.53
Processing	Viscosity (30 °C), mPa·s	88.30 ± 0.88	43.00 ± 0.43	28.00 ± 0.28	20.00 ± 0.20	17.30 ± 0.17
	Cd (35 s at 4.77 mW/cm^2), μm	343.20 ± 11.05	309.84 ± 14.14	288.35 ± 68.07	296.40 ± 15.40	156.59 ± 5.77

the literature.

3.5. Benefits of dual-curing processing

One of the main challenges in additive manufacturing through vat photopolymerization 3D printing is enhancing the mechanical properties of the available materials. High-performance mechanical materials face limitations in this process due to internal stresses caused by swelling or shrinkage of the layers, which can lead to deformations, cracks, or fractures in large-sized parts. In this study, we demonstrate that the described system does not face these limitations when creating large parts. The intermediate material of the system can withstand large deformations, between 60 % and 150 %, while maintaining an excellent resolution in the Z-axis of 0.07 mm. This opens new possibilities for manufacturing large parts with excellent mechanical properties.

Fig. 10.a shows a network formed by the RAC20AC40 system, where the intermediate material behaves flexibly. In this state, it can endure significant deformations without breaking, as seen in Fig. 10.b. Upon completion of the curing process, the material becomes rigid and can reach up to 70 MPa in tension an example Fig. 10.c. Another significant advantage of this system is the post-processing capability. After printing, the intermediate material can adopt new geometries, which is crucial for complex configurations that typically increase processing times in conventional 3D printing or avoid the use of supports. Fig. 10.d illustrates an example of a piece initially printed as a rectangle, which, after post-processing, is transformed into a circular shape. This piece then undergoes thermal treatment to acquire its final properties. Creating this piece through traditional vat photopolymerization 3D printing would require printing in horizontal position that may be not suitable for some geometries or if printing vertically, it would take much longer and supports would be needed. In both cases, it changes from minute-long print into hours. Additionally, Fig. 10.e and 10.f display two configurations created using a mold in their intermediate state, which are later fixed in their final state via thermal treatment. These intricate configurations generally require more time and the use of supports in conventional 3D printing, depending on the mechanical properties of the resins used.

Fig. 11 provides a detailed comparison of multiple systems described in the literature [20,34,50,58–65], specifically highlighting the parameters of apparent viscosity and maximum tensile strength. A significant trend is observed, with many materials from the scientific literature exhibiting considerably higher viscosities. Additionally, most evaluated commercial systems demonstrate tensile strengths below 50 MPa, with systems exceeding this threshold generally exhibiting high viscosities, which limit their versatility in industrial applications. However, our research has shown that dual-curing systems make it possible to maintain low formulation viscosity while exhibiting excellent mechanical properties, due to the use of low molecular weight components, opening new possibilities in structural applications. Specifically, the maximum tensile and shear stress of some of the formulations studied in this work are clearly superior to those of many systems reported in the literature. This is also true for the tested joints, even if some mechanical strength is lost, which could be optimized by adequately selecting the joint configuration and geometry.

4. Conclusions

A dual acrylic/epoxy curing system with low viscosity and high strain in the first stage of curing and high mechanical performance in the second stage of curing, designed for compatibility with vat photopolymerization 3D printing, was developed.

The first curing stage leads to intermediate, low Tg (meth)acrylic

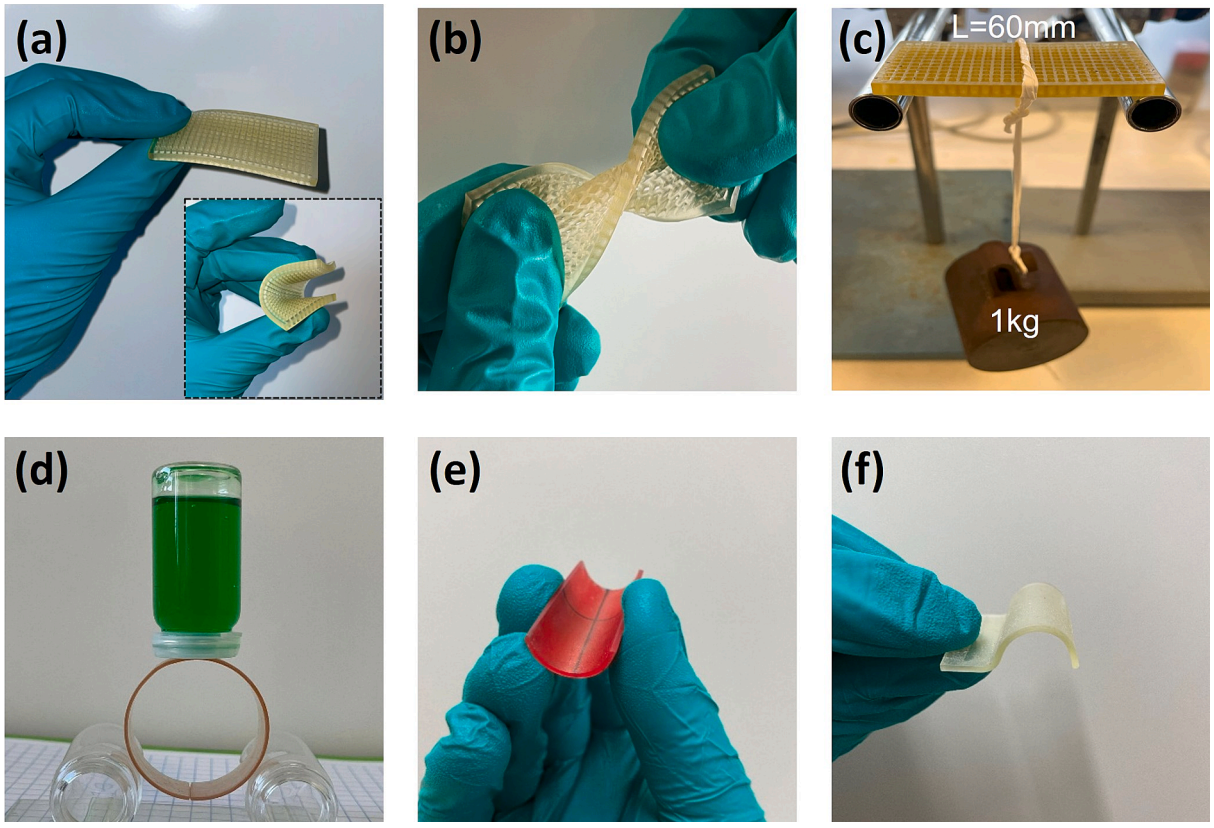

Fig. 10. (a) Net-like structure in the first printing stage, demonstrating its flexibility. (b) Net-like structure subjected to high deformations, showcasing its resilience. (c) Net-like structure in its final state, supporting a load of 1 kg. (d) Post-processed piece derived from a rectangular printed part. (e) Post-processed piece derived from a rectangular sheet (one section). (f) Post-processed piece derived from a rectangular sheet (two sections).

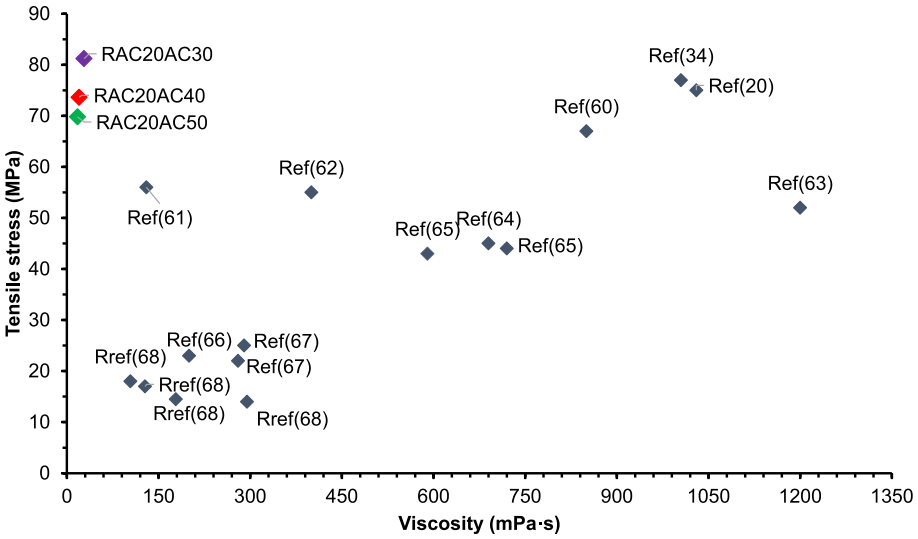

Fig. 11. Tensile stress and apparent viscosity for systems found in the literature. The gap shows the improvement of the low viscosity and high mechanical properties for some values reported in this work.

networks and high flexibility, showing elastomer-like behavior with deformations reaching up to 160 %. This remarkable behavior results from the contribution of the reduced cross-linking density of the acrylic network, which enhances stretching ability due to the presence of the coupling agent HEMA acting as a chain extender, and a moderate swelling effect of the unreacted epoxy monomer, which has in turn good compatibility with the acrylic matrix thanks to the intermolecular interactions with the side –OH groups of the coupling agent in the acrylic chains. Additionally, the intermediate state not only exhibits excellent latency and reactivity but also allows for post-processing of printed parts to achieve new geometries. This advantage is particularly beneficial in applications requiring high geometric precision, where printing without the use of supports would otherwise be impossible. Notably, this intermediate material also exhibited excellent attributes of latency and reactivity.

The second curing stage produced significant changes in the network architecture and the final thermal and mechanical properties of the materials, due to the homopolymerization of epoxy groups leading to a more densely crosslinked network structure. Final materials featured a relatively high Tg, surpassing 100 °C, which turned into rigid mechanical behavior with maximum tensile strength near to 80 MPa and deformations of approximately 7 %. The presence of the HEMA coupling agent enhanced significantly the compatibility between the acrylic and the epoxy network due to the participation of the OH groups of HEMA as chain-transfer agents in the epoxy homopolymerization via de AM mechanism, producing more uniform co-network structures.

All the formulations show low viscosity allowing an easy processing in the 3D printer. High resolution parts could be printed and easily deformed without breaking due to the high stretching ability of the intermediate materials. This allowed creation of complex shapes with enhanced mechanical strength after completion of the second curing stage. The adhesion capabilities of the dual-curing processing were also demonstrated by the mechanical analysis of tensile and shear joints, yielding comparable and decent results, both in comparison to bulk values and relative to those reported in the literature. The activation and generation of chemical bonds by residual acrylic groups and the reactive epoxy groups emerged as the factors responsible for the favorable outcomes observed in these bonded joints.

In summary, these materials feature a unique and unprecedented combination of viscosity, reactivity and final mechanical properties, which makes them highly attractive for vat 3D-printing of components for mechanically demanding applications, which can also benefit from the additional advantages of a robust multi-stage dual-curing processing with excellent control of the curing sequence, the adhesion capabilities and high deformability of the intermediate material and post-processing possibilities.

CRediT authorship contribution statement

A.A. Escriba-Flores: Writing – original draft, Visualization, Validation, Investigation, Formal analysis. **X. Fernández-Francos:** Writing – review & editing, Supervision, Resources, Project administration, Methodology, Conceptualization. **F. Ferrando:** Supervision, Conceptualization. **A. Fabregat-Sanjuan:** Writing – review & editing, Supervision, Resources, Methodology, Formal analysis, Conceptualization.

Declaration of competing interest

The authors declare the following financial interests/personal relationships which may be considered as potential competing interests: A. Escribá, X. Fernandez-Francos, and A. Fabregat-Sanjuan are holders of a pending utility model related to this work, submitted to the Spanish Patent and Trademark Office (OEPM) (Utility model: DUAL-CURED FORMULATION FOR 3D PRINTING (U 202431191)). The other authors declare no competing interests.

Acknowledgements

This work was funded by the Spanish Ministry of Science and Innovation (MCIN/AEI/10.13039/501100011033) through R&D projects PID2020-115102RB-C21 and PID2020-115102RB-C22, and also by Generalitat de Catalunya (2021-SGR-154). Armando Escribá acknowledges the Martí Franquès Research Fellowship Programme (2021PMF-BS-08). X. Fernández-Francos acknowledges the Serra-Húnter programme (Generalitat de Catalunya).

Appendix A. Supplementary data

Supplementary data to this article can be found online at https://doi.org/10.1016/j.eurpolymj.2025.113878.

Data availability

Data will be made available on request.

References

[1] Z. Guo, H. Zhang, W. Xie, A. Tang, W. Liu, 3D printing hydrogel with structural design via vat photopolymerization for strain sensing, Addit. Manuf. 77 (2023) 103824, https://doi.org/10.1016/j.addma.2023.103824.

[2] Z. Fang, R. Lu, J. Chen, Q. Zhao, J. Wu, Vat photopolymerization of tough glassy polymers with multiple shape memory performances, Addit. Manuf. 59 (2022) 103171, https://doi.org/10.1016/j.addma.2022.103171.

[3] A. Al Rashid, W. Ahmed, M.Y. Khalid, M. Koç, Vat photopolymerization of polymers and polymer composites: Processes and applications, Addit. Manuf. 47 (2021) 102279, https://doi.org/10.1016/j.addma.2021.102279.

[4] F. Zhang, L. Zhu, Z. Li, S. Wang, J. Shi, W. Tang, N. Li, J. Yang, The recent development of vat photopolymerization: A review, Addit. Manuf. 48 (2021), https://doi.org/10.1016/j.addma.2021.102423.

[5] M.B.A. Tamez, I. Taha, A review of additive manufacturing technologies and markets for thermosetting resins and their potential for carbon fiber integration, Addit. Manuf. 37 (2021) 101748, https://doi.org/10.1016/j.addma.2020.101748.

[6] J. Borrello, P. Nasser, J.C. Iatridis, K.D. Costa, 3D printing a mechanically-tunable acrylate resin on a commercial DLP-SLA printer, Addit. Manuf. 23 (2018) 374–380, https://doi.org/10.1016/j.addma.2018.08.019.

[7] S. Chen, L. Yu, S. Zhang, X. Sun, B. Qu, R. Wang, Y. Zheng, X. Liu, W. Li, J. Gao, D. Zhuo, Synergistic strengthening and toughening of 3D printing photosensitive resin by bismaleimide and acrylic liquid-crystal resin, J. Sci.: Adv. Mater. Devices 8 (2023) 8, https://doi.org/10.1016/j.jsamd.2023.100565.

[8] S. Tangpothitham, P. Pongprueksa, M. Inokoshi, S. Mitrirattanakul, Effect of post-polymerization with autoclaving treatment on monomer elution and mechanical properties of 3D-printing acrylic resin for splint fabrication, J. Mech. Behav. Biomed. Mater. 126 (2022) 105015, https://doi.org/10.1016/j.jmbbm.2021.105015.

[9] A. Bagheri, J. Jin, Photopolymerization in 3D Printing, ACS Appl. Polym. Mater. 1 (2019) 593–611, https://doi.org/10.1021/acsapm.8b00165.

[10] S. Keck, O. Liske, K. Seidler, B. Steyrer, C. Gorsche, S. Knaus, S. Baudis, Synthesis of a Liquid Lignin-Based Methacrylate Resin and Its Application in 3D Printing without Any Reactive Diluents, Biomacromolecules 24 (2023) 1751–1762, https://doi.org/10.1021/acs.biomac.2c01505.

[11] T. Siripongpreda, V.P. Hoven, B. Narupai, N. Rodthongkum, Emerging 3D printing based on polymers and nanomaterial additives: Enhancement of properties and potential applications, Eur. Polym. J. 184 (2023) 111806, https://doi.org/10.1016/j.eurpolymj.2022.111806.

[12] S. Functions, S.A.C. Resin, C. Kinetics, Development and Applications of UV-Curing 3D Printing and, Photosensitive Resin 31 (2021) 63–70, https://doi.org/10.14133/j.cnki.1008-9357.20210510001.

[13] H. Quan, T. Zhang, H. Xu, S. Luo, J. Nie, X. Zhu, Photo-curing 3D printing technique and its challenges, Bioact. Mater. 5 (2020) 110–115, https://doi.org/10.1016/j.bioactmat.2019.12.003.

[14] O. Konuray, J.M. Morancho, X. Fernández-Francos, M. García-Alvarez, X. Ramis, Curing kinetics of dually-processed acrylate-epoxy 3D printing resins, Thermochim Acta 701 (2021) 178963, https://doi.org/10.1016/J.TCA.2021.178963.

[15] A. Roig, X. Ramis, S. De la Flor, À. Serra, Dual-cured thermosets from glycydil methacrylate obtained by epoxy-amine reaction and methacrylate homopolymerization, React. Funct. Polym. 159 (2021) 104822, https://doi.org/10.1016/J.REACTFUNCTPOLYM.2021.104822.

[16] U. Shaukat, A. Thalhamer, E. Rossegger, S. Schlögl, Dual-vat photopolymerization 3D printing of vitrimers, Addit. Manuf. 79 (2024) 103930, https://doi.org/10.1016/J.ADDMA.2023.103930.

[17] M. Pagac, J. Hajnys, Q.P. Ma, L. Jancar, J. Jansa, P. Stefek, J. Mesicek, A review of vat photopolymerization technology: Materials, applications, challenges, and future trends of 3d printing, Polymers (basel) 13 (2021) 1–20, https://doi.org/10.3390/polym13040598.

[18] S.C. Ligon, R. Liska, J. Stampfl, M. Gurr, R. Mülhaupt, Polymers for 3D Printing and Customized Additive Manufacturing, Chem. Rev. 117 (2017) 10212–10290, https://doi.org/10.1021/acs.chemrev.7b00074.

[19] Z. Weng, X. Huang, S. Peng, L. Zheng, L. Wu, 3D printing of ultra-high viscosity resin by a linear scan-based vat photopolymerization system, Nat. Commun. 14 (2023) 1–9, https://doi.org/10.1038/s41467-023-39913-4.

[20] J. Zhao, Q. Li, F. Jin, N. He, Digital light processing 3D printing Kevlar composites based on dual curing resin, Addit. Manuf. 41 (2021) 101962, https://doi.org/10.1016/j.addma.2021.101962.

[21] C.M.B. Ho, S.H. Ng, K.H.H. Li, Y.J. Yoon, 3D printed microfluidics for biological applications, Lab Chip 15 (2015) 3627–3637, https://doi.org/10.1039/c5lc00685f.

[22] N.A. Rodriguez, H. Song, M. Chen, J.S. Oakdale, E.B. Duoss, C.C. Seepersad, R. H. Crawford, Use of wire grid polarizers with liquid crystal display for large-volume stereolithography, Addit. Manuf. 52 (2022) 102641, https://doi.org/10.1016/J.ADDMA.2022.102641.

[23] D.Z. Lin, P.H. Yu, Z.J. Zhang, Y.C. Chen, S.C. Lin, J.Y. Jeng, Design and fabrication of large area vat photopolymerization 3D printing system using a 32-inch quasi-collimated visible backlight module with local dimming control, Addit. Manuf. 73 (2023) 103665, https://doi.org/10.1016/J.ADDMA.2023.103665.

[24] C. Lu, Y. Liu, C. Wang, Q. Yong, J. Wang, F. Chu, An integrated strategy to fabricate bio-based dual-cure and toughened epoxy thermosets with photothermal conversion property, Chem. Eng. J. 433 (2022) 134582, https://doi.org/10.1016/j.cej.2022.134582.

[25] D. Guzmán, X. Ramis, X. Fernández-Francos, S. De la Flor, A. Serra, New bio-based materials obtained by thiol-ene/thiol-epoxy dual curing click procedures from eugenol derivates, Eur. Polym. J. 93 (2017) 530–544, https://doi.org/10.1016/j.eurpolymj.2017.06.026.

[26] A.O. Konuray, X. Fernández-Francos, X. Ramis, Curing kinetics and characterization of dual-curable thiol-acrylate-epoxy thermosets with latent reactivity, React. Funct. Polym. 122 (2018) 60–67, https://doi.org/10.1016/j.reactfunctpolym.2017.11.010.

[27] S. Moradi, X. Fernández-Francos, O. Konuray, X. Ramis, Recyclable dual-curing thiol-isocyanate-epoxy vitrimers with sequential relaxation profiles, Eur. Polym. J. 196 (2023), https://doi.org/10.1016/j.eurpolymj.2023.112290.

[28] D. Santín, O. Konuray, X. Fernàndez-Francos, X. Ramis, Kinetics analysis and simulation of sequential epoxy dual-curing systems with independent thermal activation, Thermochim Acta 673 (2019) 158–168, https://doi.org/10.1016/j.tca.2019.01.023.

[29] C. Russo, F. Bustamante, X. Fernández-Francos, S. De la Flor, Adhesive properties of thiol-acrylate-epoxy composites obtained by dual-curing procedures, Int. J. Adhes. Adhes. 112 (2022) 102959, https://doi.org/10.1016/j.ijadhadh.2021.102959.

[30] V. Dahmen, A.J. Redmann, J. Austermann, A.L. Quintanilla, S.J. Mecham, T. A. Osswald, Fabrication of hybrid composite T-joints by co-curing with 3D printed dual cure epoxy, Compos. B Eng. 183 (2020) 107728, https://doi.org/10.1016/j.compositesb.2019.107728.

[31] O. Konuray, A. Sola, J. Bonada, A. Tercjak, A. Fabregat-Sanjuan, X. Fernández-Francos, X. Ramis, Cost-Effectively 3D-Printed Rigid and Versatile Interpenetrating Polymer Networks, Materials 14 (2021) 4544, https://doi.org/10.3390/ma14164544.

[32] O. Konuray, F. Di Donato, M. Sangermano, J. Bonada, A. Tercjak, X. Fernandez-Francos, A. Serra, X. Ramis, X. Fernández-Francos, Serra, X. Ramis, Dual-curable stereolithography resins for superior thermomechanical properties, Express Polym Lett 14 (2020) 881–894. https://doi.org/10.3144/expresspolymlett.2020.72.

[33] O. Konuray, A. Altet, J. Bonada, A. Tercjak, X. Fernández-Francos, X. Ramis, Epoxy Doped, Nano-scale Phase-separated Poly-Acrylates with Potential in 3D Printing, Macromol. Mater. Eng. 306 (2021) 2000558, https://doi.org/10.1002/mame.202000558.

[34] H. Wang, Z. Huang, Y. Zhang, L. Li, J. Li, Design of enhanced mechanical properties by interpenetrating network of 3D printing dual-curing resins, Polymer (guildf) 282 (2023) 126153, https://doi.org/10.1016/j.polymer.2023.126153.

[35] L. Zhao, R. Yu, Y. He, M. Zhang, F. Tian, L. Wang, Y. Zhao, W. Huang, 3D printed epoxy/acrylate hybrid polymers with excellent mechanical and shape memory properties via UV and thermal cationic dual-curing mechanism, Addit. Manuf. 79 (2024) 103904, https://doi.org/10.1016/j.addma.2023.103904.

[36] P. Kubisa, S. Penczek, Cationic activated monomer polymerization of heterocyclic monomers, Progress in Polymer Science (oxford) 24 (1999) 1409–1437, https://doi.org/10.1016/S0079-6700(99)00028-3.

[37] M.J. Starink, The determination of activation energy from linear heating rate experiments: A comparison of the accuracy of isoconversion methods, Thermochim Acta 404 (2003) 163–176, https://doi.org/10.1016/S0040-6031(03)00144-8.

[38] A.J. Brunner, Investigating the performance of adhesively-bonded composite joints, in: Fatigue and Fracture of Adhesively-Bonded Composite Joints, Elsevier, 2015: pp. 3–42. https://doi.org/10.1016/B978-0-85709-806-1.00001-X.

[39] L. Sohier, J.Y. Cognard, P. Davies, Analysis of the mechanical behaviour of adhesively bonded assemblies of composites under tensile–shear out-of-plane loads, Compos. A Appl. Sci. Manuf. 53 (2013) 65–74, https://doi.org/10.1016/j.compositesa.2013.05.008.

[40] B. Duncan, Developments in testing adhesive joints, in: Advances in Structural Adhesive Bonding, Elsevier, 2010: pp. 389–436. https://doi.org/10.1533/9781845698058.3.389.

[41] X. Fernández, J.M. Salla, À. Serra, A. Mantecón, X. Ramis, Cationic copolymerization of cycloaliphatic epoxy resin with a spirobislactone with lanthanum triflate as initiator: I. Characterization and shrinkage, J. Polym. Sci. A Polym. Chem. 43 (2005) 3421–3432, https://doi.org/10.1002/pola.20801.

[42] I. Isarn, F. Gamardella, L. Massagués, X. Fernández-Francos, À. Serra, F. Ferrando, New epoxy composite thermosets with enhanced thermal conductivity and high Tg obtained by cationic homopolymerization, Polym. Compos. 39 (2018) E1760–E1769, https://doi.org/10.1002/pc.24774.

[43] S. Vyazovkin, D. Achilias, X. Fernandez-Francos, A. Galukhin, N. Sbirrazzuoli, ICTAC Kinetics Committee recommendations for analysis of thermal polymerization kinetics, Thermochim Acta 714 (2022) 179243, https://doi.org/10.1016/j.tca.2022.179243.

[44] A.O. Konuray, A. Ruiz, J.M. Morancho, J.M. Salla, X. Fernández-Francos, À. Serra, X. Ramis, Sequential dual curing by selective Michael addition and free radical polymerization of acetoacetate-acrylate-methacrylate mixtures, Eur. Polym. J. 98 (2018) 39–46, https://doi.org/10.1016/j.eurpolymj.2017.11.003.

[45] A.O. Konuray, X. Fernández-Francos, À. Serra, X. Ramis, Sequential curing of amine-acrylate-methacrylate mixtures based on selective aza-Michael addition followed by radical photopolymerization, Eur. Polym. J. 84 (2016) 256–267, https://doi.org/10.1016/j.eurpolymj.2016.09.025.

[46] X. Fernàndez-Francos, S.G. Kazarian, X. Ramis, À. Serra, Simultaneous Monitoring of Curing Shrinkage and Degree of Cure of Thermosets by Attenuated Total Reflection Fourier Transform Infrared (ATR FT-IR) Spectroscopy, Appl. Spectrosc. 67 (2013) 1427–1436, https://doi.org/10.1366/13-07169.

[47] O. Konuray, J.M. Salla, J.M. Morancho, X. Fernández-Francos, M. García-Alvarez, X. Ramis, Curing kinetics of acrylate-based and 3D printable IPNs, Thermochim Acta 692 (2020) 178754, https://doi.org/10.1016/j.tca.2020.178754.

[48] R. Dong, L. Wang, J. Zhu, L. Liu, Y. Qian, A novel SiO2–GO/acrylic resin nanocomposite: fabrication, characterization and properties, Appl. Phys. A 125 (2019) 551, https://doi.org/10.1007/s00339-019-2847-7.

[49] M.Z. Khan, M.H. Younes, A. Zaib, U. Farooq, A. Khan, M.D. Zahid, U. Hussan, Investigation of space charge behavior in self-healing epoxy resin composites, J. Mater. Sci. Mater. Electron. 32 (2021) 19646–19654, https://doi.org/10.1007/s10854-021-06487-0.
[50] Z. Yang, S. Peng, Z. Wang, J.-T. Miao, L. Zheng, L. Wu, Z. Weng, UV-Curable, Low-Viscosity Resin with a High Silica Filler Content for Preparing Ultrastiff, 3D-Printed Molds, ACS Appl. Polym. Mater. 4 (2022) 2636–2647, https://doi.org/10.1021/acsapm.1c01920.
[51] D.N. Lastovickova, F.R. Toulan, J.R. Mitchell, D. VanOosten, A.M. Clay, J. F. Stanzione, G.R. Palmese, J.J. La Scala, Resin, cure, and polymer properties of photopolymerizable resins containing <scp>bio-derived</scp> isosorbide, J. Appl. Polym. Sci. 138 (2021), https://doi.org/10.1002/app.50574.
[52] A. Bhat, B. Smith, C.Z. Dinu, A. Guiseppi-Elie, Dataset on hydrophobicity indices and differential scanning calorimetry thermograms for poly(HEMA)-based hydrogels, Data Brief 24 (2019) 103891, https://doi.org/10.1016/j.dib.2019.103891.
[53] G. Griffini, M. Invernizzi, M. Levi, G. Natale, G. Postiglione, S. Turri, 3D-printable CFR polymer composites with dual-cure sequential IPNs, Polymer (guildf) 91 (2016) 174–179, https://doi.org/10.1016/j.polymer.2016.03.048.
[54] X. Kuang, Z. Zhao, K. Chen, D. Fang, G. Kang, J. Qi Hang, H.J. Qi, J. Qi Hang, High-Speed 3D Printing of High-Performance Thermosetting Polymers via Two-Stage Curing, Macromol. Rapid Commun. 39 (2018) 1700809, https://doi.org/10.1002/marc.201700809.
[55] Q. Wang, G. Zhang, X. Zheng, Y. Ni, F. Liu, Y. Liu, L.R. Xu, Efficient characterization on the interlayer shear strengths of 3D printing polymers, J. Mater. Res. Technol. 22 (2023) 2768–2780, https://doi.org/10.1016/j.jmrt.2022.12.147.
[56] C. Salom, M.G. Prolongo, A. Toribio, A.J. Martínez-Martínez, I.A. de Cárcer, S. G. Prolongo, Mechanical properties and adhesive behavior of epoxy-graphene nanocomposites, Int. J. Adhes. Adhes. 84 (2018) 119–125, https://doi.org/10.1016/j.ijadhadh.2017.12.004.
[57] M.R. Khosravani, P. Soltani, T. Reinicke, Failure and fracture in adhesively bonded 3D-printed joints: An overview on the current trends, Eng. Fail. Anal. 153 (2023), https://doi.org/10.1016/j.engfailanal.2023.107574.
[58] Z. Feng, Y. Li, L. Hao, Y. Yang, T. Tang, D. Tang, W. Xiong, Graphene-Reinforced Biodegradable Resin Composites for Stereolithographic 3D Printing of Bone Structure Scaffolds, J. Nanomater. 2019 (2019) 1–13, https://doi.org/10.1155/2019/9710264.
[59] J. Guit, M.B.L. Tavares, J. Hul, C. Ye, K. Loos, J. Jager, R. Folkersma, V.S.D. Voet, Photopolymer Resins with Biobased Methacrylates Based on Soybean Oil for Stereolithography, ACS Appl. Polym. Mater. 2 (2020) 949–957, https://doi.org/10.1021/acsapm.9b01143.
[60] J.-T. Miao, S. Peng, M. Ge, Y. Li, J. Zhong, Z. Weng, L. Wu, L. Zheng, Three-Dimensional Printing Fully Biobased Heat-Resistant Photoactive Acrylates from Aliphatic Biomass, ACS Sustain. Chem. Eng. 8 (2020) 9415–9424, https://doi.org/10.1021/acssuschemeng.0c02168.
[61] Z. Weng, Y. Zhou, W. Lin, T. Senthil, L. Wu, Structure-property relationship of nano enhanced stereolithography resin for desktop SLA 3D printer, Compos Part A Appl Sci Manuf 88 (2016) 234–242, https://doi.org/10.1016/j.compositesa.2016.05.035.
[62] S. Li, Y. Cui, J. Li, Thiol-terminated hyperbranched polymer for <scp>DLP 3D</scp> printing: Performance evaluation of a low shrinkage photosensitive resin, J. Appl. Polym. Sci. 138 (2021), https://doi.org/10.1002/app.50525.
[63] Y. Luo, G. Le Fer, D. Dean, M.L. Becker, 3D Printing of Poly(propylene fumarate) Oligomers: Evaluation of Resin Viscosity, Printing Characteristics and Mechanical Properties, Biomacromolecules 20 (2019) 1699–1708, https://doi.org/10.1021/acs.biomac.9b00076.
[64] M. Porcarello, C. Mendes-Felipe, S. Lanceros-Mendez, M. Sangermano, Design of acrylated epoxidized soybean oil biobased photo-curable formulations for 3D printing, Sustain. Mater. Technol. 40 (2024) e00927, https://doi.org/10.1016/j.susmat.2024.e00927.
[65] O.W. Saadi, A. Schiffer, S. Kumar, Piezoresistive behavior of DLP 3D printed CNT/polymer nanocomposites under monotonic and cyclic loading, Int. J. Adv. Manuf. Technol. 126 (2023) 1965–1978, https://doi.org/10.1007/s00170-023-11123-8.